Available online at www.sciencedirect.com
ScienceDirect
Journal of Computational Physics 217 (2006) 485–501
JOURNAL OF COMPUTATIONAL PHYSICS
www.elsevier.com/locate/jcp

SPH simulation of transition to turbulence for planar shear flow subjected to a streamwise magnetic field

Fangming Jiang [a,*], Mónica S.A. Oliveira [a], Antonio C.M. Sousa [a,b]

[a] Departamento de Engenharia Mecânica, Universidade de Aveiro, Campus Universitário de Santiago, 3810-193 Aveiro, Portugal
[b] Department of Mechanical Engineering, University of New Brunswick, Fredericton, NB, Canada E3B 5A3

Received 22 November 2004; received in revised form 6 June 2005; accepted 7 January 2006
Available online 10 February 2006

Abstract

Active flow control of electrically conducting fluids finds growing importance in the metallurgical industry. A magnetic field applied in the streamwise direction of electrically conducting fluid flow restrains the velocity fluctuations in the transverse plane and the transition to turbulence may be delayed. The smoothed particle hydrodynamic (SPH) methodology is employed to interpret this concept. To this purpose, the onset of turbulence is related to the transitional organization of the SPH fluid particle structure or to the temporal history of the turbulence-related quantities during the early stages of the transition to turbulence. The results put in evidence the ability of a streamwise magnetic field on controlling the transition to turbulence of an electrically conducting fluid flow, i.e., the transition to turbulence may be distinctly delayed in the fluid flow subjected to a streamwise magnetic field. Furthermore, if the applied streamwise magnetic field is strong enough, the Reynolds stress in the streamwise direction may be dominant over the transverse counterpart, and turbulence is anisotropic as only in the streamwise direction of the fluid flow, the Reynolds stress is detectable.

Keywords: Smoothed particle hydrodynamics; Magnetohydrodynamics; Turbulence control; Simulation; CFD

1. Introduction

Turbulence is a complex phenomenon, which has been the object of intense research for some time. Even so, basic questions remain to be fully answered, for instance, the underlying mechanisms related to the transition of the flow regime from laminar to turbulent as the flow rate is increased are still not well-understood [1–4]. The work to be reported here does not aim to resolve this issue, but to present a novel numerical method for dealing with the control of transition to turbulence in planar shear flows from the viewpoint of magnetohydrodynamics (MHD).

Motion of electrically conducting fluids, such as liquid metals, across a magnetic field induces the so-called Lorentz force. This force, when properly handled, may suppress the flow instability and control the onset of

* Corresponding author. Tel.: +351 91 7657659; fax: +351 234 370953.
E-mail addresses: fm_jiang2000@yahoo.com (F. Jiang), asousa@unb.ca (A.C.M. Sousa).

0021-9991/$ - see front matter © 2006 Elsevier Inc. All rights reserved.
doi:10.1016/j.jcp.2006.01.009

turbulence. The original work of Hartmann and Lazarus [5] was the first one to identify the modification in drag and the suppression of turbulence when a magnetic field is applied to turbulent liquid metal flows. From then on, MHD began to arouse growing interest in metallurgical applications, in particular, to create favourable flow conditions in tundish devices, as described by Szekely and Ilegbusi [6].

A magnetic field applied in the transverse (wall-normal) direction of a fluid flow creates a ponderomotive body force and changes the mean velocity profile due to the formation of the so-called Hartmann layers [7,8] at electrically insulating boundaries normal to the magnetic field. Numerous studies with particular emphasis on the structure of the flow pattern have been addressed to the interactions between fluid flow and the applied transverse magnetic field, as cited by Lee and Choi [7]. Krasnov et al. [8] investigated the flow instability and transition to turbulence of low magnetic Reynolds number flow between two parallel electrically insulating walls. In contrast to the transverse magnetic field, a magnetic field applied in the streamwise direction does not directly interact with the mean flow, but it does restrain the turbulence fluctuations in the transverse plane of fluid flow. If the applied streamwise magnetic field is strong enough, the turbulent quantities in the transverse directions of the flow have their development prevented. The flow instability may be restrained and the transition to turbulence may be delayed, or even arrested. This work aims to interpret this concept by means of smoothed particle hydrodynamics (SPH) simulations, rather than by the commonly used Eulerian-based computational fluid dynamics (CFD), an approach, which has already demonstrated its adequacy in MHD turbulence research [7–9].

SPH is a meshless particle based Lagrangian fluid dynamics simulation technique, in which the fluid flow is represented by a collection of discrete elements or pseudo-particles. These particles are initially distributed with a specified density distribution and evolve in time according to the fluid conservation equations (e.g., mass, momentum). Flow properties are determined by an interpolation or smoothing of the nearby particle distribution using a special weighting function – the smoothing kernel. This technique was first proposed by Gingold and Monaghan [10] and Lucy [11] in the context of astrophysical modeling. It has been successful in a broad spectrum of problems, among others, heat conduction [12,13], forced and natural convective flow [14,15], low Reynolds number flow [16,17], interfacial flow [18–20], multiphase flow [21,22], viscoelastic flow [23], viscoelastic solid mechanics [24], flow in porous materials [25–28], chemically reactive flow [29], particulate flow [30], non-Newtonian flow [23,31], die casting [32,33], environmental flow [34,35], and astronomy and astrophysics [36–39]. Comprehensive reviews about the history and some advances of SPH can be found in [40,41].

In comparison to the Eulerian-based CFD method, SPH is advantageous in what concerns the following aspects: (a) particular suitability to tackle problems dealing with multiphysics; (b) ease of handling complex free surface and material interface; and (c) relatively simple computer codes and ease of machine parallelization. These advantages make it particularly well suited to deal with the problem of interest in this paper.

The reported work is organized as follows: (1) a MHD equation group is derived, and the mechanism on turbulence control is addressed; (2) a set of computer programmable SPH formulations is presented; (3) a benchmarked fluid mechanics problem is employed to test the SPH calculation code; and (4) the transition to turbulence in planar shear flows is investigated in detail by means of SPH simulations.

2. MHD modeling

The MHD flow is governed by a set of coupled partial differential equations that express the conservation of mass, momentum and the interaction between the flow and the applied magnetic field. In this paper, electrically conducting fluid flow constrained in two parallel infinite plates is considered. A uniform magnetic field is applied in the streamwise direction and the boundary plates are electrically insulated. It is assumed that the hydrodynamic Reynolds number Re is much larger than the magnetic Reynolds number Re_m, namely,

$$Re = \frac{UL}{\nu} \gg Re_m = \frac{UL}{\eta}. \tag{1}$$

Here, $\eta = (\sigma\mu_0)^{-1}$. ν, σ and μ_0 are the kinematic viscosity, electrical conductivity and magnetic permeability of the free space ($\mu_0 = 4\pi \times 10^{-7}$ H m^{-1}), respectively. U and L are the characteristic velocity and length of the

fluid flow, respectively. This assumption guarantees the fluctuations of the magnetic field due to the fluid motion are very small as compared to the applied field $\boldsymbol{B}_0$; therefore the total magnetic field can be considered uniform and time independent, and the induced electrical current $\boldsymbol{j}$ is given by

$$\boldsymbol{j} = \sigma(\nabla\varphi + \boldsymbol{V} \times \boldsymbol{B}_0), \tag{2}$$

where $\boldsymbol{V}$ is the fluid velocity vector (bold text designates vector or tensor) and φ is the induced electrical potential, which is produced by the interactions of the applied magnetic field and flow vorticity $\boldsymbol{w}$ ($=\nabla \times \boldsymbol{V}$). The present study does not aim to investigate the turbulence pattern or structure of MHD turbulent flows, as conducted in other studies [7–9], what of interest here is to investigate the early stages of the transition to turbulence; and the configuration considered here is two dimensional; for which, in practice, it is reasonable to assume that $\boldsymbol{w}$ is negligible. Furthermore, the induced electrical potential is assumed to be zero, which yields [42]:

$$\boldsymbol{j} = \sigma(\boldsymbol{V} \times \boldsymbol{B}_0). \tag{3}$$

The Lorentz force defined per unit of volume, $\boldsymbol{F}$ takes the form:

$$\boldsymbol{F} = \boldsymbol{j} \times \boldsymbol{B}_0 = \sigma(\boldsymbol{V} \times \boldsymbol{B}_0) \times \boldsymbol{B}_0. \tag{4}$$

Because $\boldsymbol{B}_0$ is aligned with the fluid stream the produced Lorentz force $\boldsymbol{F}$ has no influence on the bulk flow, but it does affect the formation of turbulent fluctuations in the transverse plane. For example, if the velocity fluctuation in the transverse plane has the magnitude of v', the force created to restrain it is $-\sigma B_0^2 v'$. This means that a strong enough magnetic field $\boldsymbol{B}_0$ can effectively inhibit the development of flow turbulence. Two-dimensional planar shear flow is chosen to interpret this concept.

As outlined above, the MHD equations for the transient 2-D (x–y) planar shear flow with the presence of a uniform, time-independent streamwise (positive x direction) magnetic field $\boldsymbol{B}_0$ are formulated as

$$\frac{\mathrm{D}\rho}{\mathrm{D}t} = -\rho\left(\frac{\partial u}{\partial x} + \frac{\partial v}{\partial y}\right), \tag{5}$$

$$\rho\frac{\mathrm{D}u}{\mathrm{D}t} = -\frac{\partial p}{\partial x} + \mu\left(\frac{\partial^2 u}{\partial x^2} + \frac{\partial^2 v}{\partial y^2}\right) + F_{\mathrm{B}x}, \tag{6}$$

$$\rho\frac{\mathrm{D}v}{\mathrm{D}t} = -\frac{\partial p}{\partial y} + \mu\left(\frac{\partial^2 u}{\partial x^2} + \frac{\partial^2 v}{\partial y^2}\right) - \sigma B_0^2 v + F_{\mathrm{B}y}, \tag{7}$$

where u and v denote the velocity components in the streamwise (x) and transverse (y) direction, respectively. For the flow of interest, u is the total velocity in x direction and v is the velocity fluctuation in the y direction. ρ and μ stand for the density and dynamic viscosity, respectively. $\mathrm{D}/\mathrm{D}t$ is the material derivative. $F_{\mathrm{B}x}$ and $F_{\mathrm{B}y}$ ($\mathrm{N/m^3}$) are the components of the body force in the x and y direction, respectively.

3. SPH formulation

In SPH, the continuous flow at time t is represented by a collection of N particles located at position $\boldsymbol{r}_i(t)$ and moving with velocity $\boldsymbol{v}_i(t)$, $i = 1, 2, \ldots, N$. The 'smoothed' value of any field quantity $q(\boldsymbol{r}, \boldsymbol{v})$ at a space point $\boldsymbol{r}$ is a weighted sum of all contributions from the neighbouring particles

$$\langle q(\boldsymbol{r}, \boldsymbol{v})\rangle = \sum_{j=1}^{N} \frac{m_j}{\rho(\boldsymbol{r}_j)} q(\boldsymbol{r}_j, \boldsymbol{v}_j) w(|\boldsymbol{r} - \boldsymbol{r}_j|, h), \tag{8}$$

$$\langle \nabla q(\boldsymbol{r}, \boldsymbol{v})\rangle = \sum_{j=1}^{N} \frac{m_j}{\rho(\boldsymbol{r}_j)} q(\boldsymbol{r}_j, \boldsymbol{v}_j) \nabla w(|\boldsymbol{r} - \boldsymbol{r}_j|, h), \tag{9}$$

where m_j and $\rho(\boldsymbol{r}_j)$ denote the mass and density of particle j, respectively. $w(|\boldsymbol{r}|, h)$ is the weight or smoothing function with h being the smoothing length. In terms of Eq. (9), the 'smoothed' version of the continuity equation, Eq. (5) is

$$\frac{\mathrm{d}\rho_i}{\mathrm{d}t} = \sum_j m_j \boldsymbol{v}_{ij} \cdot \nabla_i w_{ij}. \tag{10}$$

The summation is over all neighbouring particles j with exception of particle i itself. $\boldsymbol{v}_{ij} = \boldsymbol{v}_i - \boldsymbol{v}_j$, $\boldsymbol{r}_{ij} = \boldsymbol{r}_i - \boldsymbol{r}_j$ and $w_{ij} = w(|\boldsymbol{r}_i - \boldsymbol{r}_j|, h)$. ∇_i denotes that gradient derivatives are taken with respect to the coordinates at particle i

$$\nabla_i w_{ij} = \frac{\boldsymbol{r}_{ij}}{|\boldsymbol{r}_{ij}|} \frac{\partial w_{ij}}{\partial r_i}. \tag{11}$$

The transformation of the momentum equations, Eqs. (6) and (7), into their SPH version is relatively involved, because it requires the symmetrization of the pressure terms [15] to satisfy momentum conservation and the adequate treatment of the viscous terms. The most commonly used, symmetrized SPH expression for the pressure gradients is

$$-\left(\frac{1}{\rho}\nabla p\right)_i = -\sum_j m_j \left(\frac{p_i}{\rho_i^2} + \frac{p_j}{\rho_j^2}\right) \nabla_i w_{ij}. \tag{12}$$

The use of Eq. (12), in particular when the Lorentz force is present, may facilitate the SPH particles to clump in pairs, causing tensile instability. This numerical instability was first studied in detail by Swegle et al. [43], who related the instability to the sign of the product of the stress (or pressure for liquids) times by the second order derivative of the smoothing kernel. Numerous artifacts were attempted to eliminate or reduce this tensile instability, among others, Randles and Lisberty [41] used dissipative terms which they called conservative smoothing, Dilts [44] corrected the standard SPH by generalizing SPH with an interpolant which gives accurate derivatives, and Biessel and Belyschko [45] introduced an artificial quadratic term into their variational principle to remove the so-called short wavelength instability. More recently, Imaeda and Inutsuka [46] judged that the numerical instability encountered in their SPH implementation was due to the inaccurate solution of the continuity equation, since the standard SPH cannot ensure *local* mass conservation. They used the particle velocity, instead of the fluid velocity of the standard SPH, to update the particle positions and obtained good results.

A simple and time-saving correcting method is employed in the present work, which was proposed by Monaghan [47] and it entails the addition of a small term to the right-hand side of Eq. (12), namely

$$-\left(\frac{1}{\rho}\nabla p\right)_i = -\sum_j m_j \left(\frac{p_i}{\rho_i^2} + \frac{p_j}{\rho_j^2} + R f_{ij}^n\right) \nabla_i w_{ij}, \tag{13}$$

where

$$f_{ij} = \frac{w_{ij}}{w(\Delta p, h)}, \tag{14}$$

with Δp being the average particle spacing. The factor R depends on the pressure and density; here R is determined as

$$R = \begin{cases} \varphi_1 \dfrac{|p_i|}{\rho_i^2} & \text{if } p_i < 0, \\ \varphi_1 \dfrac{|p_j|}{\rho_j^2} & \text{if } p_j < 0, \\ \varphi_2 \left(\dfrac{p_i}{\rho_i^2} + \dfrac{p_j}{\rho_j^2}\right) & \text{if } p_i > 0 \text{ and } p_j > 0. \end{cases} \tag{15}$$

In Eq. (15), the first and second rows are the basic corrections for the tensile instability; while the last row is used to avoid the formation of local linear structures. The exponential n is dependent on the smoothing kernel, $n = w(0,h)/w(\Delta p, h)$; n is greater than zero, so in essence, the additional term in Eq. (13) represents a repulsive force that can be considered as an artificial pressure and is used to prevent the particles to clump. It is worth pointing out that this artificial pressure only takes effect when particles clump (i.e., $r_{ij} < \Delta p$), whereas it has no influence under "normal" flow conditions. The two constants φ_1 and φ_2 are

given the values of 0.5 and 0.01, respectively. Monaghan [47] used a smaller value for φ_1, $\varphi_1 = 0.2$. In the present implementation, it was demonstrated that $\varphi_1 = 0.2$ is not sufficiently large to effectively restrain the tensile instability, therefore $\varphi_1 = 0.5$ is used. The selection of n also has some flexibility. In the original work by Monaghan [47], the cubic spline kernel was used and the smoothing length h was equal to $1.3\Delta p$, thus n should be 2.2; whereas $n = 4.0$ was taken therein, which was based on the assumption of $h = \Delta p$; however, in the present work the value of n will be determined according to the formulation $n = w(0,h)/w(\Delta p,h)$.

Morris et al. [17] presented an expression to simulate the viscous diffusion:

$$\left\{\left(\frac{1}{\rho}\nabla\cdot\mu\nabla\right)\boldsymbol{v}\right\}_i = \sum_j \frac{m_j(\mu_i+\mu_j)\boldsymbol{v}_{ij}}{\rho_i\rho_j}\left(\frac{1}{|\boldsymbol{r}_{ij}|}\frac{\partial w_{ij}}{\partial r_i}\right). \tag{16}$$

This formulation does not resort to the use of the unrealistic *artificial viscosity* [40], and it avoids the direct computation of the second order derivative of the smoothing kernel [15]. Eq. (16) conserves only approximately the angular momentum [48], but this does not affect its unique accuracy for the simulations of viscous flows in straight channels [16,17,48]. The substitution of Eqs. (13) and (16) into Eqs. (6) and (7) yields the following form for the SPH momentum equations:

$$\frac{\mathrm{d}u_i}{\mathrm{d}t} = -\sum_j m_j\left(\frac{p_i}{\rho_i^2}+\frac{p_j}{\rho_j^2}+Rf_{ij}^n\right)\frac{(x_i-x_j)}{|\boldsymbol{r}_{ij}|}\frac{\partial w_{ij}}{\partial r_i} + \sum_j \frac{m_j(\mu_i+\mu_j)u_{ij}}{\rho_i\rho_j}\left(\frac{1}{|\boldsymbol{r}_{ij}|}\frac{\partial w_{ij}}{\partial r_i}\right) + F_{\mathrm{Bx}}, \tag{17}$$

$$\frac{\mathrm{d}v_i}{\mathrm{d}t} = -\sum_j m_j\left(\frac{p_i}{\rho_i^2}+\frac{p_j}{\rho_j^2}+Rf_{ij}^n\right)\frac{(y_i-y_j)}{|\boldsymbol{r}_{ij}|}\frac{\partial w_{ij}}{\partial r_i} + \sum_j \frac{m_j(\mu_i+\mu_j)v_{ij}}{\rho_i\rho_j}\left(\frac{1}{|\boldsymbol{r}_{ij}|}\frac{\partial w_{ij}}{\partial r_i}\right) - \sigma B_0^2 v_i + F_{\mathrm{By}}. \tag{18}$$

A quasi-compressible method is implemented to calculate the dynamic pressure p, in which an artificial equation of state is used [17]:

$$p = p_0\left[\left(\frac{\rho}{\rho_0}\right)^{\gamma} - 1.0\right], \tag{19}$$

where p_0 is the magnitude of the pressure for the material state being of the reference density ρ_0. To govern the weak compressibility of the fluid, a large value (7.0) is artificially attributed to the ratio of the specific heats γ. In this way, perturbations of the density field remain very small even at high Reynolds numbers. The choice of $\gamma = 7.0$ is based on the equation of state for water and it was first adopted by Monaghan [49]. A lower value of γ is also feasible in SPH simulations, e.g., $\gamma = 1.0$ as used by Morris et al. [17]. They argued that a lower value of γ gives more accurate pressure estimates and this is favourable to their SPH implementations of low Reynolds number flows. If c_s denotes the speed of sound, it can be formulated by the following expression:

$$c_s^2 = \frac{\gamma p_0}{\rho_0} = \alpha U^2, \tag{20}$$

where U is the characteristic or maximum fluid velocity. The choice of α is a compromise: it should be an adequate value to avoid making p_0 (or c_s) too large, which will force the time advancement of the simulation to become prohibitively slow, and to prevent yielding Mach numbers that violate the incompressibility condition of the fluid; α takes 100 in this paper, which ensures density variations less than 1.0%.

The XSPH variant [19] is used to guarantee the SPH particles move with a velocity consistent with the average velocity of its neighbouring particles, which is particularly favourable for the simulation of high speed flows:

$$\frac{\mathrm{d}\boldsymbol{r}_i}{\mathrm{d}t} = \boldsymbol{v}_i + \varepsilon\sum_j \frac{m_j\boldsymbol{v}_{ij}}{\bar{\rho}_{ij}}w_{ij}. \tag{21}$$

Here $\bar{\rho}_{ij} = (\rho_i+\rho_j)/2.0$ and the factor ε is chosen as $\varepsilon = 0.5$.

A direct numerical integration algorithm is used to perform the integration of Eqs. (10), (17), (18) and (21). The time step Δt is adaptive and determined by the CFL condition [17]:

$$\Delta t = \min\left(\frac{c_1 h}{\max_i(15.0U, |\boldsymbol{v}_i|)}, c_2\sqrt{\frac{h}{\text{max acceleration}}}, \frac{c_3 h}{\text{max sound speed}}\right). \tag{22}$$

The Courant "safety" factors c_1, c_2 and c_3 are given as $c_1 = 0.125$, $c_2 = 0.25$ and $c_3 = 0.25$, respectively. On the right-hand side of Eq. (22), the quantity $15.0U$ is introduced in the denominator of the first constraint to restrict it to a value comparable to the other two constraints so that all the three constraints may take effect during the calculations.

4. Smoothing kernel and boundary conditions

In the present implementation, the high order three-splines quintic kernel is used. The two-dimensional quintic kernel is defined as

$$w_{ij} = \frac{n_d}{h^2}\begin{cases} (3.0-s)^5 - 6.0(2.0-s)^5 + 15.0(1.0-s)^5 & \text{if } 0 \leqslant s < 1.0, \\ (3.0-s)^5 - 6.0(2.0-s)^5 & \text{if } 1.0 \leqslant s < 2.0, \\ (3.0-s)^5 & \text{if } 2.0 \leqslant s < 3.0, \\ 0 & \text{if } s \geqslant 3.0, \end{cases} \tag{23}$$

where $s = |\boldsymbol{r}_{ij}|/h$ and n_d is a normalization constant, which is determined by the normalization property [51] of the smoothing kernel

$$\int\int w(|\boldsymbol{r} - \boldsymbol{r}'|, h)\,\mathrm{d}r' = 1.0. \tag{24}$$

Initially, the distribution of SPH particles is set in a regular structure, and n_d takes the value of $7.0/478.0\pi$; this regular distribution is deformed to some extent as time advances. In order to assure the calculation accuracy, the value of n_d is adjusted, on a real-time basis, with Eq. (24) during the fluid flow development for all the fluid particles.

The smoothing length h is given by

$$h = \sqrt{(\Delta x)^2 + (\Delta y)^2}, \tag{25}$$

where Δx and Δy are the initial spacing in the x and y direction, respectively, between two neighbouring particles, and $\Delta x = \Delta y$. The interpolation of the field quantity with respect to one fluid particle extends to a region where around 61 neighbouring particles are included. After finalizing the smoothing kernel and smoothing length, the exponential n in Eq. (13) is calculated to be, $n \approx 1.6$.

The treatment of the solid wall boundaries is illustrated in Fig. 1. Taking into account the influence region of the employed quintic smoothing kernel, four layers of boundary particles are arranged outside of the fluid channel and parallel to the real wall boundary with the first layer $\Delta p/2$ away from the wall plane. These boundary particles have the same spatial separation Δp as fluid particles. The density of a boundary particle is set equal to the reference fluid density, ρ_0, and it remains unchanged throughout the calculation. Boundary

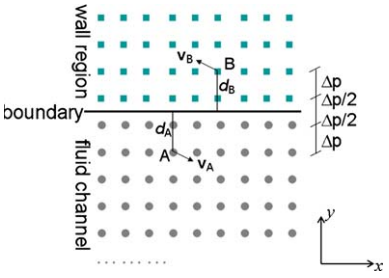

Fig. 1. Illustration of the initial particle arrangement and treatment of solid wall boundary.

particles interact with the fluid particles by contributing to their density variations, and by prescribing viscous forces on the nearby fluid particles. The boundary particle contribution to the density variation of the fluid particle implies pressure increases when fluid and boundary particle approach. The increased pressure prevents the fluid particles to penetrate the wall boundaries, and thus the no-penetrating solid wall condition is warranted. An alternative method to mimic such boundary condition is the strategy of image particles [50]: once a fluid particle 'flows' out to the wall region, its image, which is created by reflecting it with respect to the wall boundary with opposite wall-normal velocity, is used for the following calculations. This strategy was used by Libersky et al. [50] and works very well for straight channels, but introduces density errors in the presence of curved boundaries.

The non-slip wall boundary condition is guaranteed by employing the method used by Morris et al. [17], which can be dated back to the original work by Takeda et al. [48]. For each fluid particle A, the normal distance d_A to the wall is calculated and for each boundary particle B, d_B is obtained. Then an artificial velocity $\boldsymbol{v}_B = -(d_B/d_A)\boldsymbol{v}_A$ is applied to the boundary particle B with the assumption of zero velocity condition on the boundary plane itself. This artificial velocity $\boldsymbol{v}_B$ is used to calculate the viscous force applied to the nearby fluid particles, but not used to locate the boundary particle position. Boundary particles are motionless or moving at specified velocities. The relative velocity between fluid and boundary particles is

$$\boldsymbol{v}_{AB} = \boldsymbol{v}_A - \boldsymbol{v}_B = \beta \boldsymbol{v}_A, \tag{26}$$

where

$$\beta = \min\left(\beta_{max}, 1.0 + \frac{d_B}{d_A}\right), \tag{27}$$

β_{max} is used to exclude the extremely large values when fluid particles get too close to the wall. Morris et al. [17] obtained good results for $\beta_{max} = 1.5$ when simulating low Reynolds number planar shear flows. In the present study, $\beta_{max} = 7.0$ is specified, which is the largest value of β for the initial regular particle arrangement.

The periodic boundary condition is imposed in the flow direction, which means that the particles close to the right and left ends interact with each other in terms of Eqs. (10), (17), (18) and (21) due to the periodical replication of the simulated domain. If there is one particle flowing outside from one end of the calculation region, the periodicity then ensures that a new particle, which has the same flow quantities (velocity and pressure), enters inside from the other end of the calculation region, thus the number of the total particles monitored is constant.

5. Benchmark test

The test case is a classic fluid mechanics benchmark – the Couette flow between two parallel infinite plates located at $y = -d$ and $y = d$, respectively, as shown in Fig. 2. The system is initially at rest. At time $t = 0$, the upper plate starts to move at constant velocity U_0 along the positive x-axis. Concurrently, an additional body force F_B (m/s^2) is aligned parallel to the x-axis too. The resultant velocity profile is dependent on a non-dimensional quantity, designated as χ

$$\chi = \frac{d^2\rho}{\mu U_0}(F_B), \tag{28}$$

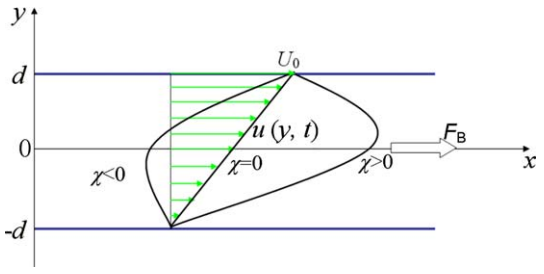

Fig. 2. Test case: Couette flow.

and its time-dependent series solution is

$$u(y,t) = \frac{F_B}{2v}(d^2 - y^2) - \sum_{n=0}^{\infty}(-1)^n \frac{16F_B d^2}{v\pi^3(2n+1)^3}\cos\left(\frac{\pi y}{2d}(2n+1)\right)\exp\left(-\frac{(2n+1)^2\pi^2 v}{4d^2}t\right) + \frac{U_0}{2d}(y+d) + \sum_{n=1}^{\infty}(-1)^n \frac{2U_0}{n\pi}\sin\left(\frac{n\pi}{2d}(y+d)\right)\exp\left(-\frac{n^2\pi^2 v}{4d^2}t\right). \quad (29)$$

The first two terms in the right-hand side of Eq. (29) designate the contribution from the applied body force F_B and the last two result from the motion of the upper plate. When time t approaches infinite, the steady state solution takes the form:

$$u(y,\infty) = \frac{\chi}{2}U_0\left(1 - \frac{y^2}{d^2}\right) + \frac{1}{2}U_0\left(1 + \frac{y}{d}\right). \quad (30)$$

The flow is simulated using SPH for $v = 0.01\ \mathrm{m^2\ s^{-1}}$, $d = 0.5\ \mathrm{m}$, $\rho = 1000.0\ \mathrm{kg\ m^{-3}}$ and $U_0 = 0.2\ \mathrm{m\ s^{-1}}$. The body force F_B takes the values 0.08, 0.04, 0.016, 0.0 and $-0.008\ \mathrm{m\ s^{-2}}$, yielding normalized values for χ of 10.0, 5.0, 2.0, 0.0 and -1.0, respectively. Fifty fluid particles were set to span the flow channel and the periodic boundary pair is applied in the flow direction. The velocity profiles at time $t = 9.43$ s and time t approaching infinite are shown in Figs. 3 and 4, respectively. The largest deviation between SPH simulation and series

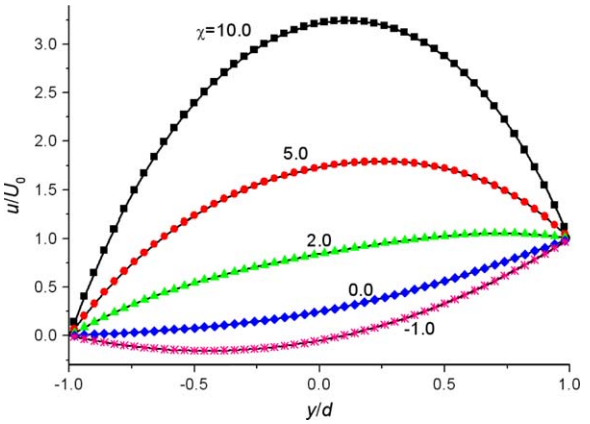

Fig. 3. Velocity profiles for Couette flow at time $t = 9.43$ s. (Lines denote series solutions, and the symbols represent SPH simulation results.)

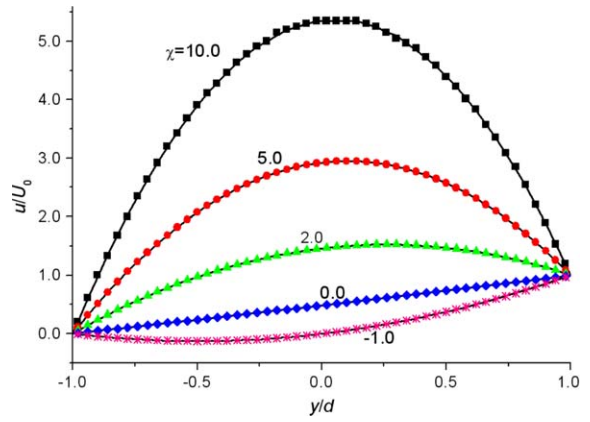

Fig. 4. Velocity profiles for Couette flow at time t approaching infinite. (Lines denote series solutions, and the symbols represent SPH simulation results.)

solution is observed at the position close to the motionless wall, even so, which is less than 1.0%. Therefore, the overall agreement between simulations and exact analytical solutions is excellent. The actual asymptotic time for the case shown in Fig. 4 is 37.73 s when all the velocity values are within 97.0% of their final steady values.

6. Transitional organization of the SPH particles versus the onset of turbulence

Cleary and Monaghan [52] studied the transition to turbulence in planar Poiseuille flow via SPH simulations. They managed to correlate the onset of turbulence to the ordered–disordered transition of the SPH fluid particles. Here, with the similar geometry and the same initial flow conditions, their work will be replicated. This effort may be looked as a further test procedure on the SPH algorithm outlined earlier on, and it is also necessary to use these results to evaluate the effect of the applied streamwise magnetic field acting on the MHD fluid flow.

A Poiseuille flow between two parallel infinite plates with a separation distance of $L = 1.0$ m is considered. Periodic boundaries in the flow direction (x) and solid boundaries confining the flow in the transverse direction (y) are specified. For low Reynolds number laminar flow, the periodic boundary constraint in the flow direction is correct; whereas for large Reynolds number flow, the artificial periodicity imposed in the x direction, to some extent, postpones the transition to turbulence. In order to reduce the influence caused by the artificial periodicity on the onset of flow turbulence, the computational domain for high Reynolds number flow is extended to a $3\text{ m} \times 1\text{ m}$ region, while for low Reynolds number laminar flow is taken a unit square ($1\text{ m} \times 1\text{ m}$) as used in [52]. The simulation is commenced with the fluid moving to the right (positive x) at unit velocity. No static pressure or body force is applied. The fluid motion is then restrained by the viscous forces. The Reynolds number is defined as $Re = UL/\nu$, with U, L being the characteristic velocity (1.0 m/s) and length (1.0 m), respectively, and the kinematic viscosity ν is adjusted to realize Poiseuille flows of different Reynolds numbers. The initial arrangement of the SPH particles and the treatment of solid wall boundaries were already illustrated in Fig. 1. Fifty fluid particles are set to span the flow channel.

Fig. 5 shows four snapshots of the flow pattern for $Re = 100$. Three columns of particles are highlighted to show the evolution of the boundary layers and to indicate the flow pattern. (Three repetitive geometric units are depicted in terms of the periodic boundary condition in the x direction.) As expected, the laminar parabolic velocity profile develops gradually. The growth in the thickness of the boundary layers is clearly visible at the early stages of the flow development. At about $t = 2.6$ s (Fig. 5(c)), the boundary shear effect propagates to the center of the channel. Afterwards, the only change in the flow pattern is the continuing cumulative attenuation in the marker particles front. Although the displacement in the streamwise direction between adjacent rows of particles is cumulative with time, the flow is stable and the fluid particles remain ordered for the entire duration of the simulation (up to 20 s). No non-negligible motion is detected in the transverse direction, as expected for laminar planar Poiseuille flow. Similar flow scenarios were also described by Cleary and Monaghan [52].

Poiseuille flow for $Re = 10^4$ is obtained with a reduced viscosity. The corresponding flow patterns are exhibited in Fig. 6. During the early transient development, the flow is stable and a flow pattern similar to plug flow sets in. At time $t = 1.06$ s (Fig. 6(a)), the top and bottom two layer of particles are sheared from the bulk flow which is still moving to the right at unit velocity. All SPH fluid particles are ordered in a flat profile. The boundary layers are very thin and can be represented by the top and bottom 2–3 layers of particles. At around $t = 1.33$ s (Fig. 6(b)), the structure of the SPH particles are seemingly ordered still. By $t = 1.64$ s (Fig. 6(c)), the ordered structure of the SPH particles is deformed to some extent in the transverse flow direction. At $t = 1.84$ s (Fig. 6(d)), clearly disordered SPH particle organization appears. Non-negligible velocity fluctuations exist in both the streamwise and transverse directions. The lines of the marker particles are still visible, which indicates that the average velocity profile is uniform. The motion is characterized by plug flow with velocity fluctuations superimposed. Since the Poiseuille flow for $Re = 100$ does not show any signs of this kind of ordered–disordered transition on the structure of SPH particles even for a much longer calculation time, it is reasonable to ascribe this transition to the onset of turbulence.

In order to assess whether there is any connection between this phenomenon and the burst of turbulence, the mean velocity profile $\bar{u}$ and the velocity correlations: $\bar{u'u'}$ and $\bar{v'v'}$ are calculated. This is done by dividing

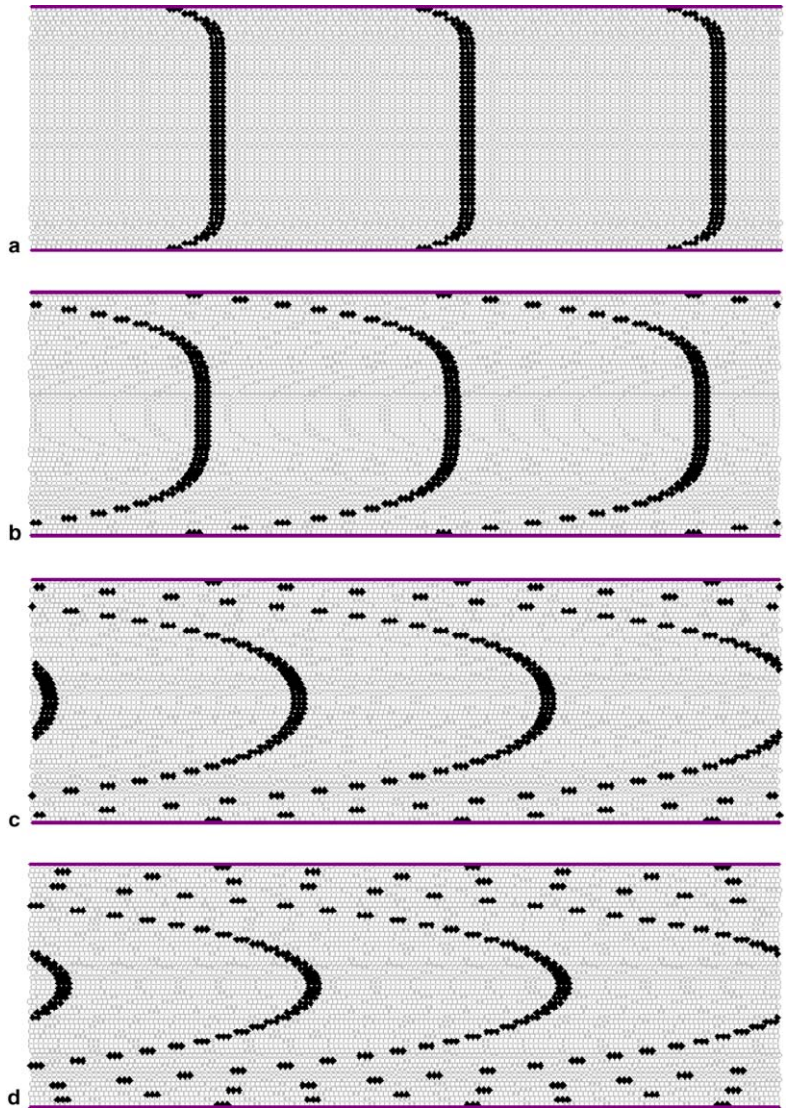

Fig. 5. Flow pattern of Poiseuille flow for $Re = 100$, at (a) time = 0.24 s, (b) time = 1.18 s, (c) time = 2.60 s, and (d) time = 3.77 s.

the flow domain into 50 horizontal stripes and by using a smaller time step to redo the calculations around time = 1.71 s; then, the results are averaged both spatially and temporally over each sub-region. These results are plotted in Fig. 7, and clearly, the flow takes the characteristics relevant to turbulent flows. The mean velocity profile is approaching to that of plug flow, i.e., occurrence of very thin boundary layers. The two velocity correlations have similar profiles except that the $\bar{v}'v'$ takes the value of zero at the walls. The turbulence sets in and the symmetry with respect to the x-axis is no longer followed. Qualitatively, these observations agree with the results reported by Cleary and Monaghan [52] too.

The influence from the SPH particle resolution is studied by examining the dependence of the calculated turbulence-related quantities ($\bar{u}'u'$ and $\bar{v}'v'$) on the SPH particle resolution. For this purpose, with respect to the same fluid flow, a Richardson extrapolation for the turbulence-related quantity as a function of 1/(number of SPH particles) was computed, based on the SPH particle resolution of 150×50, 120×40 and 240×80, respectively. The obtained SPH results with the first particle resolution, which is employed to obtain the results presented in this article, deviate from the extrapolated values by 4.2% for the $\bar{v}'v'$ and 8.3% for the $\bar{u}'u'$ at time $t = 0.81$ s; by 29.1% for the $\bar{v}'v'$ and 31.4% for the $\bar{u}'u'$ at time $t = 1.71$ s. The relatively larger error

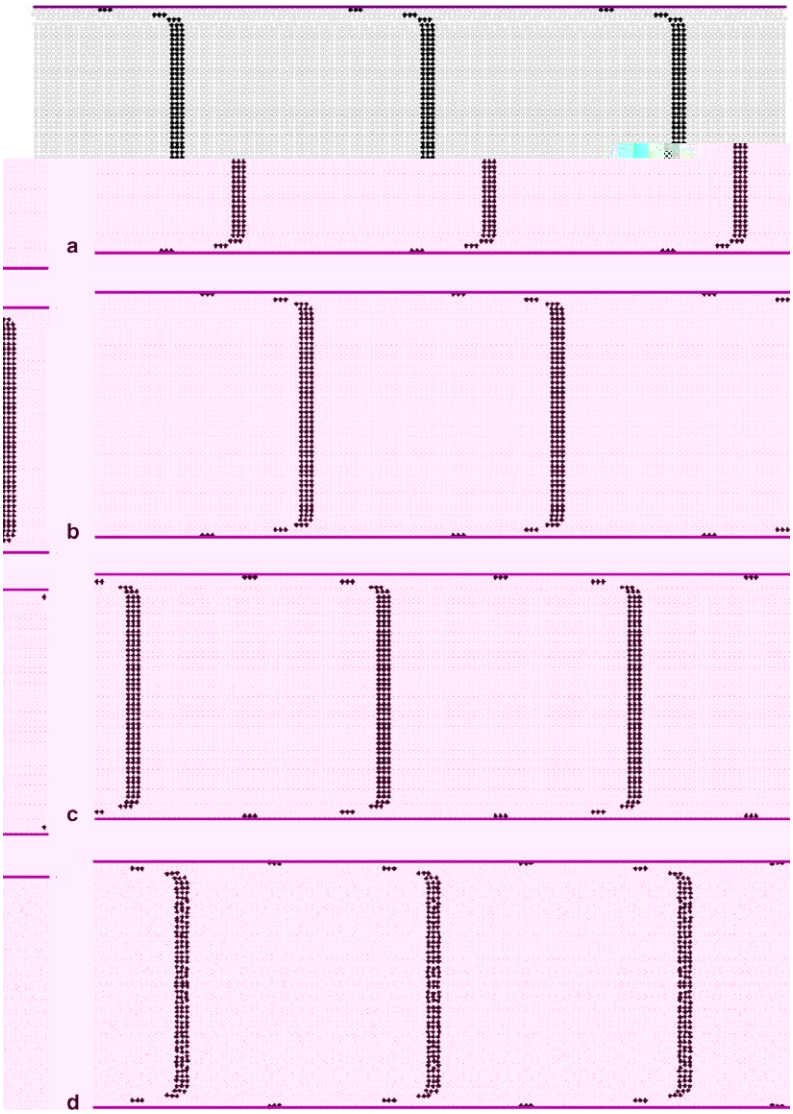

Fig. 6. Flow pattern of Poiseuille flow for $Re = 10^4$, at (a) time = 1.06 s, (b) time = 1.33 s, (c) time = 1.64 s, and (d) time = 1.84 s.

for the x velocity correlation $\bar{u}'u'$ is due to the fact that its values are smaller (several orders of magnitude smaller at time $t = 0.81$ s!) than those for $\bar{v}'v'$. More reliable SPH predictions are obtained at the early stages of the flow turbulence. A finer SPH particle resolution gives the same SPH transitional organization as shown in Fig. 6, while the boundary layers are better resolved and it yields an earlier time for the onset of turbulence.

7. MHD turbulence control with a streamwise magnetic field

As indicated by Fig. 6, the transition to turbulence for the planar shear flow seems to happen in the following sequence: (1) the viscous force restricts the fluid flow to form very thin boundary layers close to the wall boundaries; (2) disturbances erupting in the boundary layers cause velocity fluctuations in the transverse direction of the fluid flow; (3) these fluctuations transport momentum from the transverse flow direction to the streamwise direction; and, (4) once the fluctuations propagate everywhere in the fluid, the structure of the SPH particles is completely destroyed and turbulence is fully developed. A streamwise magnetic field has no influence on the bulk flow, but it does restrain the formation of velocity fluctuation in the transverse flow

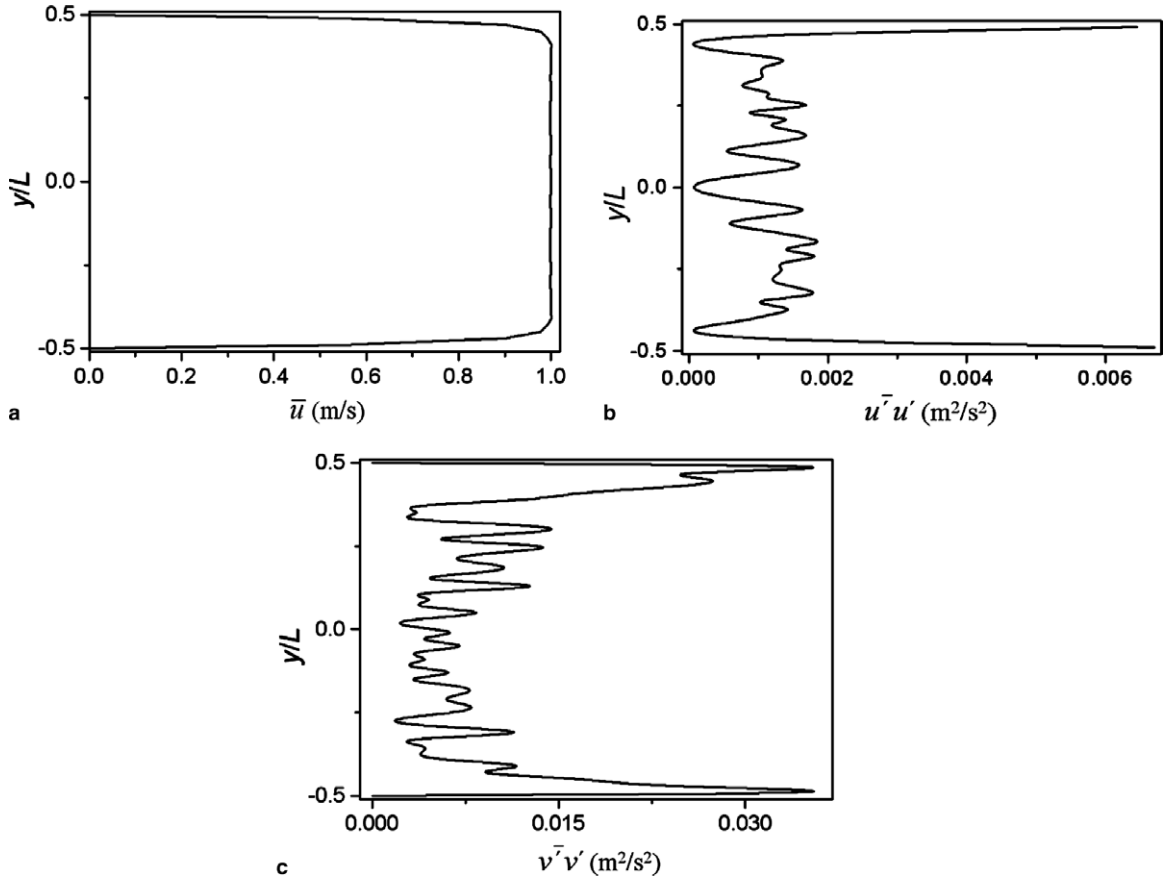

Fig. 7. Representations of (a) $\bar{u}$, (b) $\bar{u'u'}$, and (c) $\bar{v'v'}$ for Poiseuille flow of $Re = 10^4$ at time ~1.71 s.

direction. An applied streamwise magnetic field, therefore, is thought to be effective on the turbulence control for the planar shear flow, which is to be justified by applying a streamwise magnetic field to the above-mentioned planar Poiseuille shear flow for $Re = 10^4$.

Since the derivation of Eq. (3) assumes the flow vorticity is negligible; and the employed "limited" SPH particle resolution can only ensure reliable predictions during the early stages of the flow turbulence, the present study on MHD turbulence flow only considers the early stage of the transition to turbulence. Two streamwise magnetic fields that give electromagnetic forces of $\boldsymbol{F} = -4.0 \times 10^4 \boldsymbol{v}$ and $\boldsymbol{F} = -4.0 \times 10^6 \boldsymbol{v}$, respectively, are involved. Fig. 8 shows two flow patterns which are plotted from the SPH results of MHD flows imposed by these two magnetic fields, respectively. The flow patterns take on a plug flow profile with very thin boundary layers represented by 2–3 fluid particles close to the walls. Both flow patterns indicate that the SPH fluid particles are still ordered up to the observation time.

The corresponding mean velocity profile $\bar{u}$ and the velocity correlations: $\bar{u'u'}$ and $\bar{v'v'}$ are also calculated; the results are plotted in Figs. 9 and 10, respectively. These plots quantitatively describe the flow state. The mean velocity profile observed in both these two figures resembles that of plug flow. In Fig. 9, the velocity fluctuations in the x and y direction are comparable, but both at a very low level (10^{-4} m/s), which reveals that the flow turbulence, in practice, does not happen until the end of the simulation time, 1.89 s. In Fig. 10, because a stronger magnetic field is applied, even the observation time is extended by 1.79 s, it can be noted that the velocity fluctuation in the y direction gets effectively controlled and is restrained below 10^{-3} m/s still; whereas the counterpart in the x direction is gradually detectable with an explicit value of 0.05 m/s. The turbulence starts to set in. Both Figs. 9(b) and 10(b) display the maximum velocity fluctuation in the x direction appears in the central region of the flow passage. This is in contrast to what shown in Fig. 7(b), where there is

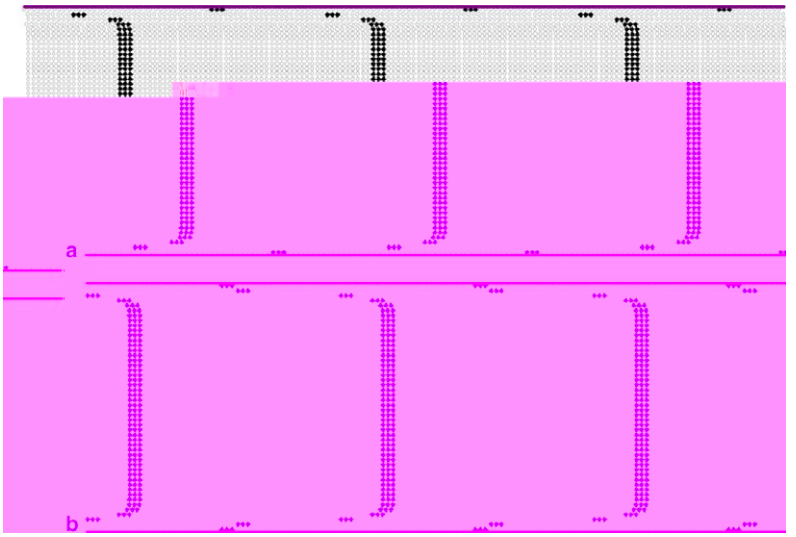

Fig. 8. Flow patterns of MHD Poiseuille flow for $Re = 10^4$, with an applied streamwise magnetic field giving electromagnetic force (a) $\boldsymbol{F} = -4.0 \times 10^4 \boldsymbol{v}$ at time = 1.89 s and (b) $\boldsymbol{F} = -4.0 \times 10^6 \boldsymbol{v}$ at time = 3.68 s, respectively.

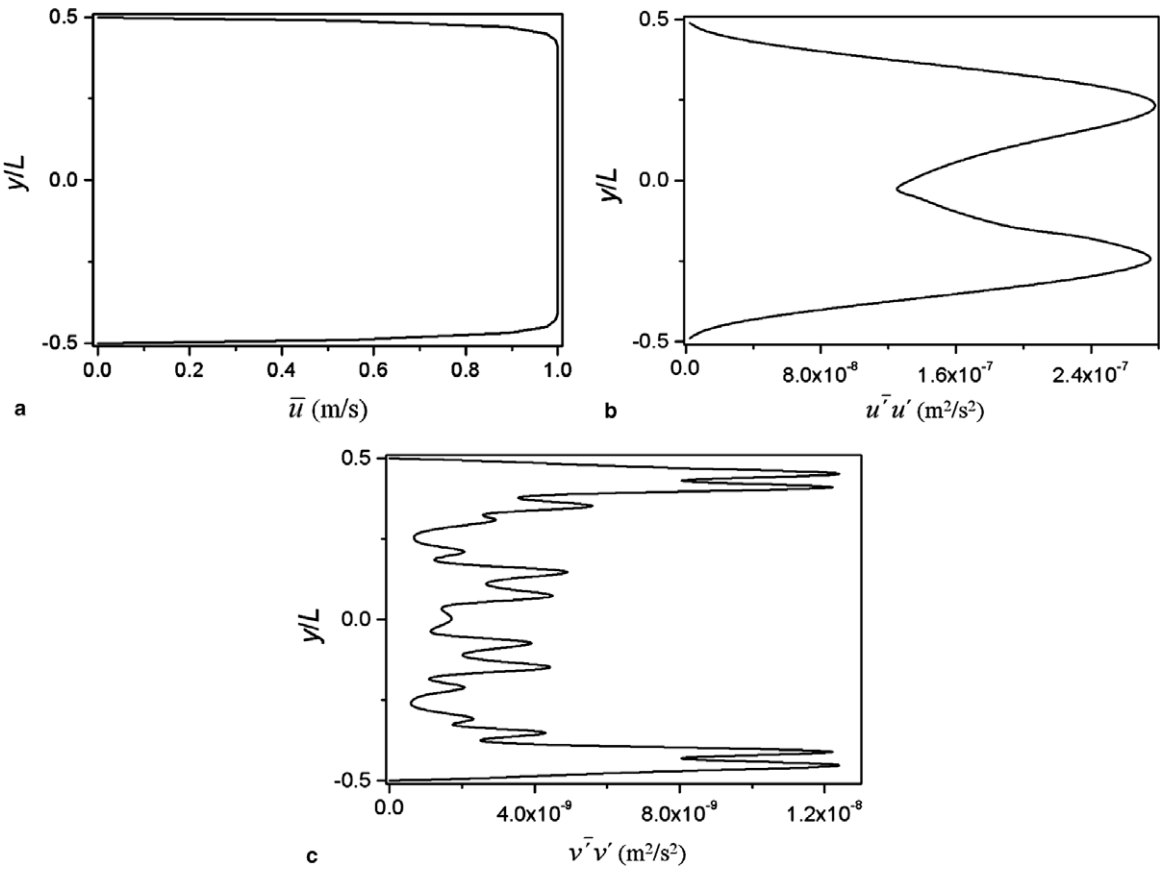

Fig. 9. Representations of (a) $\bar{u}$, (b) $\bar{u'u'}$, and (c) $\bar{v'v'}$ for Poiseuille flow of $Re = 10^4$ and with an electromagnetic force $\boldsymbol{F} = -4.0 \times 10^4 \boldsymbol{v}$ at time ~1.89 s.

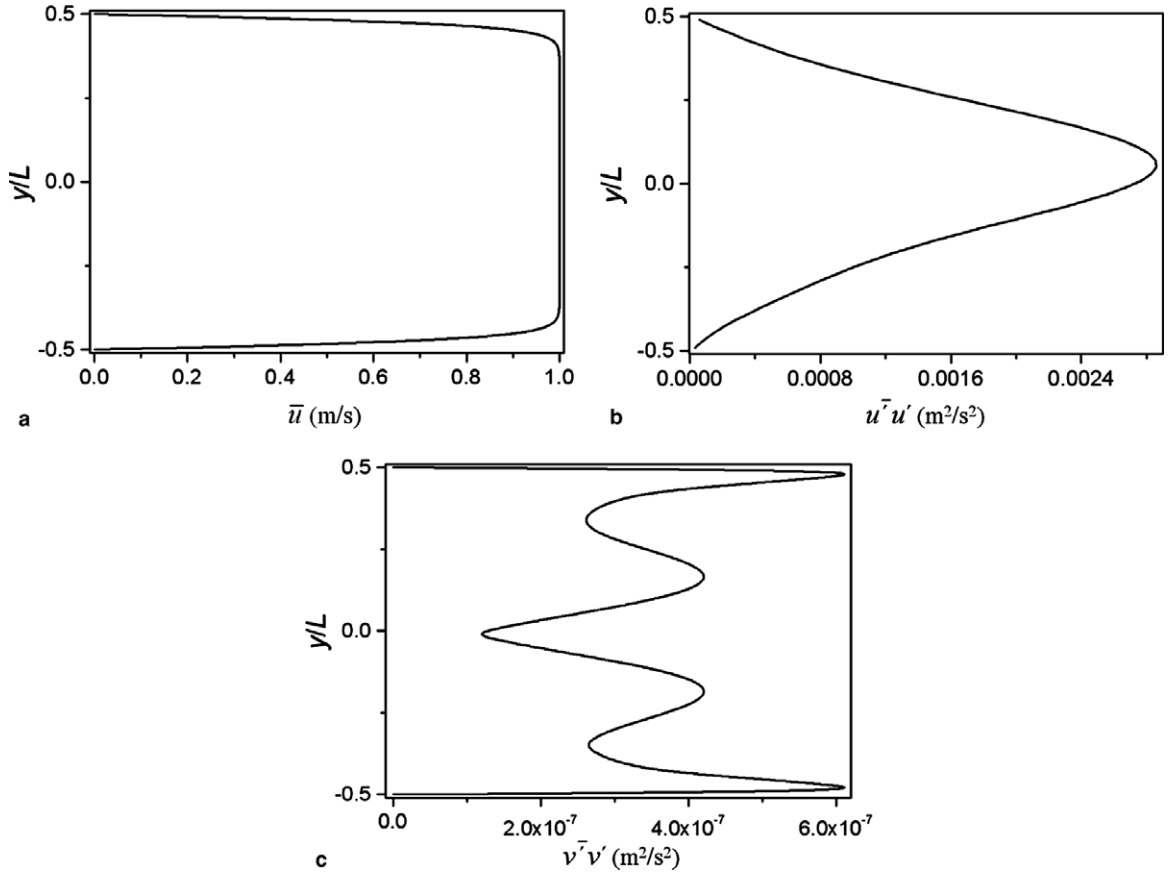

Fig. 10. Representations of (a) $\bar{u}$, (b) $\bar{u'u'}$, and (c) $\bar{v'v'}$ for Poiseuille flow of $Re = 10^4$ and with an electromagnetic force $\boldsymbol{F} = -4.0 \times 10^6 \boldsymbol{v}$ at time ~3.68 s.

no magnetic force to restrain the transverse velocity fluctuations, therefore the streamwise velocity fluctuations are substantially the result of the flow disturbance arising from the boundary layers.

Fig. 11 depicts the temporal history of $\bar{u'u'}$ and $\bar{v'v'}$ at position $y = 0.01$ m for the aforementioned three fluid flows for $Re = 10^4$, the first of which has no magnetic field applied; the second has an applied streamwise

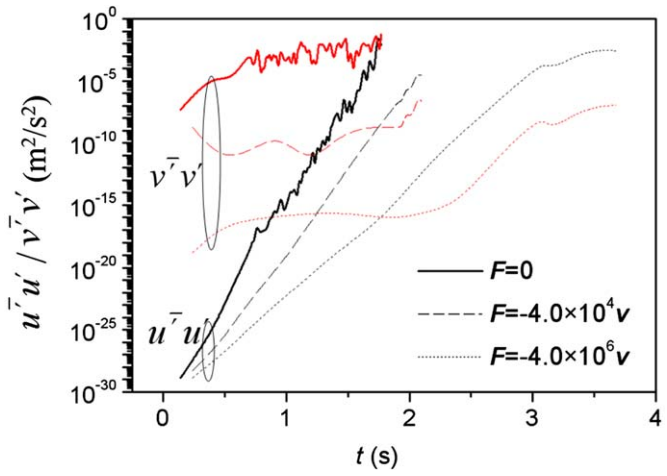

Fig. 11. The temporal history of turbulence-related velocity correlations at the position of $y = 0.01$ m for the fluid flow of $Re = 10^4$, with different magnetic field conditions.

magnetic field giving an electromagnetic force of $\boldsymbol{F} = -4.0 \times 10^4 \boldsymbol{v}$; the third has an imposed electromagnetic force of $\boldsymbol{F} = -4.0 \times 10^6 \boldsymbol{v}$. The fluid flow without magnetic field applied has the highest transverse velocity fluctuations, which transport the turbulence energy to the streamwise direction; the streamwise velocity fluctuations quickly rise to a higher level; the turbulence grows at a fast rate. An applied streamwise magnetic field effectively constrains the development of the transverse velocity fluctuations, thus it delays the onset of turbulence. By observing the variation trends of the x and y velocity correlations for the MHD fluid flow of an electromagnetic force of $\boldsymbol{F} = -4.0 \times 10^6 \boldsymbol{v}$, it can be predicted that the turbulence may still take place at a later time; however, when the turbulence occurs, the dominant velocity fluctuation (turbulence stress) is in the x direction; therefore, the turbulence is anisotropic. Qualitatively agreeable results about the turbulence control effect of a streamwise magnetic field applying to a MHD fluid flow were also reported by Lee and Choi [7].

8. Conclusion

The methodology to control the transition to turbulence of electrically conducting fluid flow with a streamwise magnetic field was fully reported. SPH simulations were performed for two-dimensional planar shear flows with and without the presence of a streamwise magnetic field. The onset of turbulence makes the SPH fluid particles experience an ordered–disordered transition, revealed by their arrangement. Because the turbulent fluctuations in the transverse plane of flow are effectively restrained by the induced electromagnetic force, the transition to turbulence is distinctly delayed for fluid flow subjected to a streamwise magnetic field. The SPH simulations with respect to the early stages of the transition to turbulence of the MHD flow describe well this concept. For the MHD flow with a sufficiently strong applied streamwise magnetic field, the Reynolds stress in the transverse direction may be controlled below a very low level, and even if the turbulence still occurs, it may be anisotropic as only in the streamwise direction of the fluid flow, the Reynolds stress is detectable.

Acknowledgments

The authors gratefully acknowledge the support received from the FCT (Foundation for Science and Technology, Portugal) Research Grant POCTI/EME/59728/2004, NSERC (Natural Sciences and Engineering Research Council of Canada) Discovery Grant 12875 (ACMS) and the Post-Doctoral Fellowship, SFRH/BPD/20273/2004 (FJ). They also acknowledge the significant contribution to the scientific quality of this work made by the reviewers.

References

[1] S. Grossmann, The onset of shear flow turbulence, Rev. Modern Phys. 72 (2000) 603.
[2] B. Hof, A. Juel, T. Mullin, Scaling of the turbulence transition threshold in a pipe, Phys. Rev. Lett. 91 (2003) 244502.
[3] H. Faisst, B. Eckhardt, Sensitive dependence on initial conditions in transition to turbulence in pipe flow, J. Fluid Mech. 504 (2004) 343.
[4] R. Rubinstein, M. Choudhari, Statistical prediction of laminar-turbulent transition, ICASE Report, vol. 39, 2000.
[5] J. Hartmann, F. Lazarus, Experimental investigations on the flow of mercury in a homogeneous magnetic field, K. Dan Vidensk Selsk. Mat. Fys. Medd. 15 (1937) 7.
[6] J. Szekley, O.J. Ilegbusi, The Physical and Mathematical Modeling of Tundish Operations, Springer, Berlin, 1989.
[7] D. Lee, H. Choi, Magnetohydrodynamic turbulence flow in a channel at low magnetic Reynolds number, J. Fluid Mech. 439 (2001) 367.
[8] D.S. Krasnov, E. Zienicke, O. Zikanov, T. Boeck, A. Thess, Numerical study of the instability of the Hartmann layer, J. Fluid Mech. 504 (2004) 183.
[9] H.-C. JI, R.A. Gardner, Numerical analysis of turbulence pipe flow in a transverse magnetic field, Int. J. Heat Mass Transfer 40 (1997) 1839.
[10] R.A. Gingold, J.J. Monaghan, Smoothed particle hydrodynamics: theory and application to non-spherical stars, Mon. Not. Roy. Astron. Soc. 181 (1977) 375.
[11] L.B. Lucy, A numerical approach to the testing of the fission hypothesis, Astronom. J. 82 (1977) 1013.
[12] P.W. Cleary, J.J. Monaghan, Conduction modelling using smoothed particle hydrodynamics, J. Comput. Phys. 148 (1999) 227.
[13] J.H. Jeong, M.S. Jhon, J.S. Halow, J. van Osdol, Smoothed particle hydrodynamics: applications to heat conduction, Comput. Phys. Commun. 153 (2003) 71.

[14] P.W. Cleary, Modeling confined multi-material heat and mass flows using SPH, Appl. Math. Modell. 22 (1998) 981.
[15] A.K. Chaniotis, D. Poulikakos, P. Koumoutsakos, Remeshed smoothed particle hydrodynamics for the simulation of viscous and heat conducting flow, J. Comput. Phys. 182 (2002) 67.
[16] L.D.G. Sigalotti, J. Klapp, E. Sira, Y. Melean, A. Hasmy, SPH simulations of time-dependent Poiseuille flow at low Reynolds numbers, J. Comput. Phys. 191 (2003) 602.
[17] J.P. Morris, P.J. Fox, Y. Zhu, Modeling low Reynolds number incompressible flows using SPH, J. Comput. Phys. 136 (1997) 214.
[18] S. Nugent, H.A. Posch, Liquid drops and surface tension with smoothed particle applied mechanics, Phys. Rev. E 62 (2000) 4968.
[19] J.P. Morris, Simulating surface tension with smoothed particle hydrodynamics, Int. J. Numer. Meth. Fluids 33 (2000) 333.
[20] A. Colagrossi, M. Landrini, Numerical simulation of interfacial flows by smoothed particle hydrodynamics, J. Comput. Phys. 191 (2003) 448.
[21] J.J. Monaghan, A. Kocharyan, SPH simulation of multi-phase flow, Comput. Phys. Commun. 87 (1995) 225.
[22] L. Cueto-Felgueroso, I. Colominas, G. Mosqueira, F. Navarrina, M. Casteleiro, On the Galerkin formulation of the smoothed particle hydrodynamics method, Int. J. Numer. Meth. Eng. 60 (2004) 1475.
[23] M. Ellero, M. Kroger, S. Hess, Viscoelastic flows studied by smoothed particle hydrodynamics, J. Non-Newtonian Fluid Mech. 105 (2002) 35.
[24] S.E. Hieber, J.H. Walther, P. Koumoutsakos, Remeshed smoothed particle hydrodynamics simulation of the mechanical behaviour of human organs, J. Technol. Health Care 12 (2004) 305.
[25] M.L. Sawley, P.W. Cleary, J. HA, Modeling of flow in porous media and resin transfer moulding using smoothed particle hydrodynamics, in: Second International Conference on CFD in the Minerals and Process Industries, Melbourne, Australia, December 1999.
[26] Y. Zhu, P.J. Fox, Smoothed particle hydrodynamics model for diffusion through porous media, Trans. Porous Media 43 (2001) 441.
[27] Y. Zhu, P.J. Fox, Simulation of pore scale dispersion in periodic porous media using smoothed particle hydrodynamics, J. Comput. Phys. 182 (2002) 622.
[28] Y. Zhu, P.J. Fox, J.P. Morris, A pore scale numerical model for flow through porous media, Int. J. Numer. Anal. Meth. Geomech. 23 (1999) 881.
[29] A.K. Chaniotis, C.E. Frouzakis, J.C. Lee, A.G. Tomboulides, D. Poulikakos, K. Boulouchos, Remeshed smoothed particle hydrodynamics for the simulation of laminar chemically reactive flows, J. Comput. Phys. 191 (2003) 1.
[30] T. Sugino, S. Yuu, Numerical analysis of fine powder flow using smoothed particle method and experimental verification, Chem. Eng. Sci. 57 (2002) 227.
[31] S. Shao, E.Y.M. Lo, Incompressible SPH method for simulating Newtonian and non-Newtonian flows with a free surface, Adv. Water Resour. 26 (2003) 787.
[32] P. Cleary, J. Ha, V. Alguine, T. Nguyen, Flow modelling in casting processes, Appl. Math. Modell. 26 (2002) 171.
[33] P.W. Cleary, J. HA, Three dimensional modelling of high pressure die casting, in: Second International Conference on CFD in the Minerals and Process Industries, Melbourne, Australia, December 1999.
[34] M.X. Rodriguez-Paz, J. Bonet, A corrected smooth particle hydrodynamics method for the simulation of debris flows, Numer. Meth. Partial Diff. Eqns. 20 (2003) 140.
[35] H.T. Shen, J. Su, L. Liu, SPH simulation of river ice dynamics, J. Comput. Phys. 165 (2000) 752.
[36] K. Dolag, M. Bartelmann, H. Lesch, SPH simulations of magnetic fields in galaxy clusters, Astron. Astrophys. 348 (1999) 351.
[37] R. Speith, H. Riffert, The viscous gas ring as an astrophysical test problem for a viscous SPH-code, J. Comput. Appl. Math. 109 (1999) 231.
[38] D.J. Price, J.J. Monaghan, Smoothed particle magnetohydrodynamics I. Algorithms and tests in one dimension, Mon. Not. Roy. Astron. Soc. 348 (2004) 123.
[39] D.J. Price, J.J. Monaghan, Smoothed particle magnetohydrodynamics II. Variational principles and variable smoothing length terms, Mon. Not. Roy. Astron. Soc. 348 (2004) 139.
[40] J.J. Monaghan, Smoothed particle hydrodynamics, Annu. Rev. Astron. Astrophys. 30 (1992) 543.
[41] R.W. Randle, L.D. Libersky, Smoothed particle hydrodynamics: some recent improvements and applications, Appl. Mech. Eng. 139 (1996) 375.
[42] J.P. Holman, Heat Transfer (seventh ed.), Chapter 12: Special Topics in Heat Transfer, McGraw-Hill Publishing Company, New York, 1990.
[43] J. Swegle, D.L. Hicks, S.W. Attaway, Smoothed particle hydrodynamics stability analysis, J. Comput. Phys. 116 (1995) 123.
[44] G.A. Dilts, Moving least squares particle hydrodynamics. I. Consistency and stability, Los Alamos Nat. Lab. Rep. LA. UR97 4168, 1996.
[45] S. Beissel, T. Belychenko, Nodal integration of the element-free Galerkin method, Comput. Meth. Appl. Mech. Eng. 139 (1996) 49.
[46] Y. Imaeda, S. Inutsuka, Shear flows in smoothed particle hydrodynamics, Astrophys. J. 569 (2002) 501.
[47] J.J. Monaghan, SPH without a tensile instability, J. Comput. Phys. 159 (2000) 290.
[48] H. Takeda, S.M. Miyama, M. Sekiya, Numerical simulation of viscous flow by smoothed particle hydrodynamics, Progr. Theor. Phys. 92 (1994) 939.
[49] J.J. Monaghan, Simulating free surface flows with SPH, J. Comput. Phys. 110 (1994) 399.
[50] L.D. Libersky, A.G. Petschek, T.C. Carney, J.R. Hipp, F.A. Allahdadi, High strain Lagrangian hydrodynamics: a three-dimensional SPH code for dynamic material response, J. Comput. Phys. 109 (1993) 67.

[51] M.B. Liu, G.R. Liu, K.Y. Lam, Constructing smoothing functions in smoothed particle hydrodynamics with applications, J. Comput. Appl. Math. 155 (2003) 263.
[52] P.W. Cleary, J.J. Monaghan, Boundary interactions and transition to turbulence for standard CFD problems using SPH, in: 6th International Computational techniques and Applications, Canberra, vol. 157, 1993.